Spectroscopy of Tm3+-doped CaF2 waveguiding thin films grown by Liquid Phase Epitaxy

Pavel Loiko, Gurvan Brasse, Liza Basyrova, Abdelmjid Benayad, Jean-Louis Doualan, Cesare Meroni, A. Braud, Elena Dunina, Alexey Kornienko, Mikhail Baranov, et al.

Spectroscopy of Tm^{3+}-doped CaF_2 waveguiding thin films grown by Liquid Phase Epitaxy

Pavel Loiko[a], Gurvan Brasse[a], Liza Basyrova[a], Abdelmjid Benayad[a], Jean-Louis Doualan[a], Cesare Meroni[a], Alain Braud[a], Elena Dunina[b], Alexey Kornienko[b], Mikhail Baranov[c], Gozhalskii Daniil[c], and Patrice Camy[a,*]

[a]*Centre de recherche sur les Ions, les Matériaux et la Photonique (CIMAP), UMR 6252 CEA-CNRS-ENSICAEN, Université de Caen Normandie, 6 Boulevard du Maréchal Juin, 14050 Caen Cedex 4, France*
[b]*Vitebsk State Technological University, 72 Moskovskaya Ave., 210035 Vitebsk, Belarus*
[c]*ITMO University, 49 Kronverkskiy Pr., 197101 Saint-Petersburg, Russia*

**Corresponding author, e-mail: patrice.camy@ensicaen.fr*

Abstract. Thulium-doped calcium fluoride (Tm:CaF_2) single-crystalline films are grown on (100)-oriented undoped bulk CaF_2 substrates by Liquid Phase Epitaxy (LPE) using LiF as a solvent. Their spectroscopic properties are studied in details. For ~2 at.% Tm-doped films, the active ions are predominantly isolated and are located in oxygen-assisted trigonal sites, $C_{3v}(T_2)$. With increasing the Tm doping level, ion clustering is promoted but it is slowed down as compared to bulk crystals. For ~6 at.% Tm-doped films, the majority of active ions form clusters resulting in a "glassy-like" spectroscopic behavior (smooth and broad spectral bands). For such layers, the maximum stimulated-emission cross-section for the $^3F_4 \rightarrow {}^3H_6$ transition is 0.14×10^{-20} cm^2 at 1856 nm, the luminescence lifetime of the $^3F_4$ state is 21.70 ms and the emission bandwidth exceeds 180 nm. The transition probabilities of Tm^{3+} ions are determined using the Judd-Ofelt theory. The waveguiding properties of the Tm:CaF_2 films are confirmed. Highly-doped Tm:CaF_2 epitaxial films are promising for waveguide lasers at ~2 μm.

Keywords: Liquid phase epitaxy; calcium fluoride; thulium ions; Raman spectra; optical spectroscopy; luminescence.

1. Introduction

Thulium ions (Tm^{3+}) are attractive for laser emission in the eye-safe spectral range of ~2 μm owing to the $^3F_4 \rightarrow {}^3H_6$ 4f-4f transition [1]. Due to the large Stark splitting of the ground-state ($^3H_6$), Tm^{3+}-doped materials exhibit broad spectral bands making them attractive for broadly tunable [2] and mode-locked lasers [3]. Tm^{3+} ions can be easily excited at ~0.8 μm, e.g., by AlGaAs laser diodes [4]. Owing to the efficient cross-relaxation (CR) process for neighboring Tm^{3+} ions, this pump scheme can lead to a quantum efficiency of 2 (one-for-two process) [5]. Tm lasers are of interest for molecular spectroscopy, range-finding, soft material processing, medicine and further frequency conversion into mid-IR.

Tm waveguide lasers benefit from compact design, small mode areas leading to low laser thresholds and high intracavity intensity and they are promising for sensing applications. So far, Liquid Phase Epitaxy (LPE) was recognized as a powerful method to fabricate single-crystalline oriented Tm^{3+}-doped active layers [6-8] exhibiting high optical quality and low propagation losses (down to 0.1 dB/cm) [9]. Tm^{3+}-doped LPE films can be used in the planar waveguide geometry or, after an additional microstructuring step [5,10], in the channel one. So far, laser-active Tm^{3+}-doped single-crystalline films based on oxide [6,8,9] and fluoride [10] materials were fabricated.

Among the host matrices for Tm^{3+} doping, fluoride crystals attracted a lot of attention [11-14]. This is because of a combination of their good thermal and spectroscopic properties. Calcium fluoride (CaF_2) is one example. As a host matrix, it provides high thermal conductivity (~9.7 $Wm^{-1}K^{-1}$) [15], isotropic thermal expansion, broadband transparency and low refractive index [16]. When doped with Tm^{3+} ions, it exhibits smooth and broad spectral bands (a "glassy-like" behavior), long upper-laser-level ($^3F_4$) lifetime and efficient CR [1]. This spectroscopic behavior is due to the strong clustering of active ions resulting in inhomogeneous broadening of spectral bands [17]. So far, efficient bulk Tm:CaF_2 lasers were demonstrated [18,19].

CaF_2 appears as an attractive material for waveguide applications. Its growth process by the Czochralski method is well-developed [20] and undoped oriented substrates are well available at reasonable costs (note that CaF_2 is a widely-used material for optical components). CaF_2 can be doped with rare-earth ions (RE^{3+}) up to relatively high concentrations which is accompanied by an increase of the refractive index [21], so that RE^{3+}:CaF_2 / CaF_2 homoepitaxies show light guiding [22]. The isotropic and attractive thermal properties of CaF_2 alleviate the thermal effects.

However, so far, the homoepitaxial growth of RE^{3+}-doped CaF_2 films has not been deeply studied. In the early studies, undoped CaF_2 films were grown on semiconducting substrates (e.g., (100) or (111) oriented Si (mainly), GaAs or InP) by molecular beam epitaxy (MBE) [23-25]. The selection of silicon was because of the relatively close lattice constants of Si and CaF_2, so that the latter was used as a buffer layer for further deposition steps. Later on, RE^{3+}:CaF_2 films (where RE = Nd, Er, Yb or Pr) were grown on (100) oriented CaF_2 substrates also by MBE [26-29]. However, the grown layers had a thickness of only few μm. The LPE growth of Yb^{3+}- and Tm^{3+}-doped CaF_2 layers was first reported in [30,31] and first laser operation was achieved in Yb:CaF_2 thin-films in the planar waveguide geometry [22].

Very recently, we reported on the LPE growth of high-optical quality Tm:CaF_2 layers with a thickness up to ~100 μm and a doping level up to ~6 at.% by LPE using lithium fluoride (LiF) as a solvent [32]. As compared to earlier studies where $CaCl_2$ was used for the same purpose [30,31], LiF is less corrosive that helps to preserve the integrity of metallic parts of the growth set-up, and it is less hygroscopic. In the present work, we report on the detailed spectroscopic study of LPE-grown Tm:CaF_2 films and, in particular, we focus on the effect of Tm doping level on the preferable site symmetry for active ions in such films that greatly affects their emission properties.

2. Growth of single-crystalline films

Single-crystalline Tm^{3+}-doped calcium fluoride (CaF_2) thin-films were grown on oriented undoped bulk CaF_2 substrates by Liquid Phase Epitaxy using lithium fluoride (LiF) as a solvent [32]. The molar composition of 65% LiF – (35 – *x*)% CaF_2 – *x*% TmF_3 was used. The starting reagents were LiF (purity: >99.5%), CaF_2 (99.5%) and Tm_2O_3 (4N). TmF_3 was achieved by fluorination of the Tm_2O_3 precursor. Two initial compositions with *x* = 5 mol% and 1.67 mol% were studied. The substrates were cut from high optical grade undoped CaF_2 wafers (Crystran, Ltd) with their surface oriented along the (100) crystallographic plane. They had a thickness of 2.0 mm and lateral dimensions of ~10×30 mm^2. Both surfaces of the substrates were polished to laser-grade quality. We have selected this substrate orientation to facilitate the LPE process in analogy to the growth of bulk CaF_2 crystals for which the preferred growth direction is along the [100] direction. In previous studies of molecular beam epitaxy of rare-earth doped CaF_2 films, particularly (100) oriented CaF_2 substrates were also used [21].

For the LPE growth, the raw materials were weighted according to the molar composition and well mixed. The batch was placed in a glassy carbon crucible which was then heated up to 900 °C and kept at this temperature for several hours under mechanical stirring leading to homogenization of the melt. The experimental saturation temperature was in the range of 854 - 856 °C (for *x* = 5 mol%) and 820 °C with a step cooling to 815 °C at a rate of 2 °C/min (for *x* = 1.75 mol%). The substrate was dipped almost vertically in the molten bath and rotated at a rate of 10 revolutions per minute (r.p.m.). The growth duration was 45 min (*x* = 5 mol%) or 70 min (*x* = 1.75 mol%) resulting in a measured film thickness of up to 85 μm (depending on the sample). To avoid the formation of unwanted (translucent) oxyfluoride phase, the growth chamber was sealed to a good secondary vacuum (~10^{-6} mbar) and filled with Ar. After completing the growth, the epitaxy was removed from the flux and slowly cooled down to room temperature (RT, ~20 °C).

The as-grown layers were transparent and colorless. On their surface, residual solvent (LiF) was crystallized during the epitaxy cooling which was easily removed by polishing.

The actual doping concentration of Tm^{3+} ions (with respect to Ca^{2+}) was calculated using the segregation coefficient previously reported [32], K_{Tm} = 0.40±0.05, and it amounted to ~6 at.% Tm (*x* = 5 mol%) and ~2 at.% Tm (*x* = 1.75 mol%).

3. Experimental

The morphology of the films was studied using a scanning electron microscope (SEM, MERLIN, Carl Zeiss). This microscope was equipped with an X-max 80 Oxford detector and used for Energy Dispersive X-ray (EDX) analysis of the film composition. A thin (27 nm) layer of carbon was deposited on the sample for this aim. The acceleration voltage was 10 keV and the spatial resolution for EDX mapping was ~30 nm.

The optical observation of the polished epitaxy was performed using a confocal scanning laser microscope (LSM 710, Carl Zeiss) equipped with ×20 and ×50 objectives, a blue GaN laser (405 nm) and a set of crossed polarizers.

The spectroscopic studies were first performed at RT (293 K). The Raman spectra were measured using a confocal microscope (inVia, Renishaw) equipped with a ×50 objective (Leica) and an Ar^+ ion laser (488.0 nm).

The absorption spectra were measured using a spectrophotometer (Lambda 1050, Perkin Elmer). The luminescence excitation spectra around 0.8 μm were measured using a tunable Ti:Sapphire laser, a monochromator (HRS2, Jobin-Yvon), a lock-in amplifier (SR810 DSP, Stanford Research Systems) and an InGaAs detector. The luminescence spectra were measured using an optical spectrum analyzer (OSA, Yokogawa AQ6375B) employing a Ti:Sapphire laser tuned to 765 nm as excitation source. The luminescence decays were detected by using a ns optical parametric oscillator (Horizon, Continuum) as pump source, a 1/4 m monochomator (Oriel 77200), two InGaAs detectors and an 8 GHz digital oscilloscope (DSA70804B, Tektronix).

For low-temperature (LT, 12 K) absorption and luminescence studies, the epitaxies were mounted on an APD DE-202 closed-cycle cryo-cooler equipped with an APD HC 2 Helium vacuum cryo-compressor and a Laceshore 330 temperature controller. A silver paint was used for thermal contact between the sample and the holder. The spectral resolution for LT measurements was 0.2 nm.

The waveguiding properties of the Tm:CaF_2 film were studied by coupling the light from a Ti:Sapphire laser (3900S, SpectraPhysics) operating in TEM_{00} mode and tuned to 770 nm. The pump was focused using a spherical CaF_2 lens (f = 40 mm) resulting in a pump spot size of 30 ± 5 μm. The guided mode was detected with a CCD camera (BladeCam-XHR, DataRay Inc.) using another CaF_2 lens (f = 15 mm).

4. Results and Discussion

4.1. Film morphology

The phase purity (cubic, sp. gr. O^5_h – $Fm\bar{3}m$, No. 225) of the grown films and their growth direction along the [100] axis was confirmed by single-crystal X-ray diffraction and their low mosaicity – by the reciprocal space mapping, similarly to [32]. For the ~6 at.% Tm-doped film, the lattice constant a_{film} = 5.4806 Å and the relative lattice mismatch $|\Delta a/a_{substrate}|$ is 0.15%.

In our previous study [32], we investigated the film morphology only by optical methods. In the present work, we employed SEM for this aim. Typical SEM images of raw (as-grown) top surface of the film doped with ~6 at.% Tm are shown in Fig. 1(a-c). In the μm-scale, Fig. 1(a), one can see crystalline layers overlaying each other with well-developed rectangular-

shaped borders, as well as small (<100 nm) nanocrystallites with squared cross-sections (from the top view) that appear as building blocks of these layers (they are interpreted as crystallization nuclei). This morphology brings to mind the cubic pattern of the natural fluorite. In larger scale, as shown in Fig. 1(b), one can see the smooth surface of the film containing "valleys" with a characteristic size of tens of μm with smooth edges and stepped hills. The residual solvent (LiF) is strongly localized within such "valleys". In larger scale, Fig. 1(c), the surface is like a hilly landscape typical for LPE-grown fluorides [33].

After polishing of the top surface of the film, in some samples, we observed crazing resulting in formation of rectangular-shaped pattern with characteristic dimensions of hundreds of μm, Fig. 1(d). This phenomenon seems to be affected by several factors: (i) thickness of the film (it is less probable in thinner films), (ii) Tm doping level (it is more probable in highly-doped films, due to distortion of the crystal lattice and the related mismatch of the lattice parameter with respect to the substrate) and (iii) growth temperature and probably cooling conditions. A very similar pattern was previously observed in CaF_2 films grown by molecular beam epitaxy (MBE) on (001) oriented InP substrates [34] and it was related to the change in the lattice mismatch at the growth and room temperatures. In our case, the lattice mismatch is relatively weak and other factors, such as stresses in the film induced by Tm^{3+} doping, may play a role.

Let us further discuss these observations in light of the previous results on the LPE growth of CaF_2. So far, the growth of epitaxial CaF_2 films on (111), (110), (100) and (001) oriented substrates (typically, semiconductors, Si or GaAs) was reported [23-25]. Among them, the easiest growth occurs orthogonal to the (111) plane as it corresponds to the minimum free energy [23] and the surface morphology is determined by small triangular hillocks [24] (the (111) plane is the perfect cleavage plane of CaF_2). The growth on the (100) oriented substrates is more complicated as films are prone to (111) faceting and columnar growth. However, these undesired effects can be avoided by a proper temperature regime [24,25]. In our case, the use of the same material for the substrate (CaF_2) reduces the lattice mismatch and eliminates the effect of the thermal expansion difference between the substrate and the layer. Using chemical etching of CaF_2 / (100) Si LPE films, Schowalter *et al*. observed rectangular symmetry of the cracks originating from dislocations and square shape of the pits revealing the (100) symmetry [23] which agrees with our observations. Siskos *et al.* observed crazing of films grown on (100) GaAs resulting in cross-hatched lines on the surface [35] (the crack directions were identified as projections of the (111) cleavage plane on the substrate surface, i.e., [011] and [$01\bar{1}$], as in our case). A similar conclusion was also made in [36] for the growth on (100) Si.

Figure 2 shows a typical SEM image of the end-facet of an epitaxially grown layer of ~6 at.% Tm:CaF_2 layer, which is relatively thin (thickness: $t = 9\pm1$ μm). It reveals a clear layer / substrate interface and a uniform, single-crystalline and crack-free layer.

The distribution of Tm^{3+} ions across the layer was analyzed by means of EDX mapping, see Fig. 3. The chemical elements constituting the epitaxy (Ca, F, Tm) were traced across the end-facet resulting in the profiles shown in Fig. 3(a). The analysis allowed us to estimate the thickness of the layer / substrate interface to be 0.4±0.1 μm indicating a weak diffusion of the

dopant (Tm) into the substrate. The EDX map for Tm, see Fig. 3(b), confirms the uniform distribution of the dopant across the active layer.

The Tm:CaF_2 epitaxial films were further studied using confocal laser microscopy in transmission mode, see Fig. 4. A ~6 at.% Tm-doped film which exhibited almost no signs of crazing was observed. First, the top surface of the film was only slightly lapped to remove the residual solvent (LiF). It exhibited a hilly landscape topography, Fig. 4(a), similar to that revealed by SEM. After polishing the top surface, Fig. 4(b), the film appeared to be uniform and crack-free (few dark lines originate from the polishing imperfections). Then, the polished end-facet was also observed, Fig. 4(c), revealing a uniform and free of crack layer (thickness: $t = 46\pm1$ μm) with a clear layer / substrate interface. The same area was also observed in crossed polarizers. This approach helps to visualize stresses in the epitaxy. No significant stresses are observed in the layer, except for the area adjacent to the layer/ substrate interface which appears to be brighter thus indicating certain stress.

4.2. Raman spectra

For the Raman study, we used the ~6 at.% Tm:CaF_2 / CaF_2 epitaxy, Fig. 5. The first-order phonon spectrum of undoped CaF_2 contains only one Raman-active vibration (symmetry: T_{2g}) [37]. Indeed, for the substrate, only one line at ~321 cm^{-1} is observed (its full width at half maximum, FWHM, is ~10 cm^{-1}). The spectra of the layer measured from the top and side surfaces are similar and contain the same line at 321 cm^{-1}. With respect to the substrate, the line for the layer is broadened (FWHM ~12 cm^{-1}) and reduced in intensity which agrees with the previous observations [38].

Other features are broad bands centered at 157, 285, 371 and 720 cm^{-1}. Russel identified similar bands in the Raman spectra of CaF_2 crystals as second-order vibrations [37], however, Gee *et al*. assigned them to luminescence of impurity rare-earth ions [39]. We assign these bands to the luminescence of the Tm^{3+} dopant (the $^1G_4 \rightarrow {}^3H_6$ transition). One may argue that the additional Raman response may originate from the residual LiF. To clarify this, we measured the Raman spectrum of a LiF powder revealing no prominent details except for an extremely weak band at ~630 cm^{-1} which can be assigned to second-order phonon processes or impurity modes [40,41].

4.3. Optical absorption

For absorption studies, we used a ~6 at.% Tm:CaF_2 / CaF_2 epitaxy (concentration of Tm^{3+} ions: $N_{Tm} = 8.28\times10^{20}$ cm^{-3}). It comprised layers on both sides of the substrate (total thickness: $t = 83\pm5$ μm).

The RT absorption spectrum, Fig. 6(a), contains Tm^{3+} ion bands related to transitions from the ground-state ($^3H_6$) to excited-states (from $^3F_4$ to $^1D_2$). The absorption bands are smooth and broad (a "glassy-like" behavior). To explain it, let us shortly describe the doping mechanism of CaF_2. Tm^{3+} ions in CaF_2 replace Ca^{2+} cations and an interstitial fluorine anion (F^-) is thus required for charge compensation. At low doping levels (<0.1 at.%) in bulk crystals, the Tm^{3+} ions are predominantly isolated and there exist several sites with different local symmetries (cubic – O_h, tetragonal – C_{4v} or trigonal – C_{3v}), depending on the location of the F^-

anion [17,42]. As electric dipole (ED) transitions are forbidden in an undistorted O_h field, the absorption spectra are mainly dominated by transitions of isolated Tm^{3+} ions in C_{3v} and C_{4v} sites. For even moderate doping levels in bulk crystals (>1 at.%), Tm^{3+} ions form clusters [43] leading to significant inhomogeneous broadening of their spectral bands. From the measured absorption spectrum, we suggest that a strong ion clustering is observed in the ~6 at.% Tm-doped film.

In Fig. 6(b,c), we focus on the absorption bands corresponding to the $^3H_6 \rightarrow {}^3H_4$ and $^3H_6 \rightarrow {}^3F_4$ transitions and calibrated in terms of absorption cross-sections and compare them with those of bulk Tm:CaF_2 crystals with low (0.05 at.%) and high (4.5 at.%) doping levels containing predominantly isolated ions and clusters, respectively. The shape of the absorption bands for ~6 at.% Tm:CaF_2 film resembles that for highly-doped bulk crystal, but they are broadened and reduced in intensity. The difference in spectral shape may be explained by (i) different geometry of clusters, (ii) possible presence of minor fraction of isolated ions and (iii) structure imperfections in thin crystalline layers affecting the local crystal-field. The difference in intensity may originate from the error in the Tm^{3+} doping concentration.

For the $^3H_6 \rightarrow {}^3H_4$ pump transition, the maximum absorption cross-section for Tm^{3+} ions in the film σ_{abs} is 0.29×10^{-20} cm^2 at 786 nm with an absorption bandwidth (FWHM) of 17 nm, compare with $\sigma_{abs} = 0.46\times10^{-20}$ cm^2 and FWHM = 13 nm for bulk 4.5 at.% Tm:CaF_2 crystal. For the $^3H_6 \rightarrow {}^3F_4$ transition of Tm^{3+} ions in the film, $\sigma_{abs} = 0.28\times10^{-20}$ cm^2 at 1614 nm.

It was difficult to measure directly the absorption spectra of ~2 at.% Tm-doped films. Thus, the RT luminescence excitation spectra were detected, Fig. 7. The excitation spectrum for the ~2 at.% Tm-doped layer contains a broad and smooth band with a maximum at 768 nm and a set of narrower lines at longer wavelengths centered at 785, 793, 799 and 805 nm. For the ~6 at.% Tm-doped layer, the same spectral features are observed while the relative intensity of the band at 768 nm greatly increases and the excitation spectrum resembles that for a bulk 4.5 at.% Tm:CaF_2 crystal studied for comparison which contains predominantly Tm^{3+} ion clusters. Thus, we assign the absorption lines at 785 – 805 nm to another type of sites which fraction decreases when increasing the Tm doping level in the layer (isolated centers). These lines are not found in the excitation spectrum of a bulk 0.05 at.% Tm:CaF_2 crystal studied for comparison, indicating different assemblage of Tm^{3+} species in the epitaxial layer. The nature of the isolated Tm^{3+} centers in epitaxial layers will be further discussed in Section 4.5.

The LT absorption spectra were measured for the ~6 at.% Tm:CaF_2 layer and compared with those for a bulk Tm:CaF_2 crystal exhibiting Tm^{3+} ion clustering. The spectra for Tm^{3+} ions in the epitaxial layer are smooth and broad at 12 K, indicating significant inhomogeneous broadening. The spectra resemble those for the bulk crystal suggesting the presence of clusters in the ~6 at.% Tm-doped layer.

Let us have a closer look at two absorption bands trying to find the signatures of isolated centers. As discussed above, the $^3H_6 \rightarrow {}^3H_4$ transition in absorption revealed the presence of possible residual isolated centers even at RT. The corresponding extra peak is split at LT resulting in three sharp lines at 791.5, 792.5 and 793.6 nm, Fig. 8(c).

As pointed out above, in bulk Tm:CaF_2 crystals, one of the possible site symmetries for isolated ions is O_h (cubic). The undistorted O_h sites are centro-symmetric ones. The presence

of a center of inversion implies that the ED transitions are forbidden, unless they are vibrationally induced. The MD transitions are however allowed for the O_h sites. For Tm^{3+} ions, the transition with a MD contribution is the $^3H_6 \rightarrow {}^3H_5$ one. The single absorption line corresponding to O_h sites is easily found in the spectrum of the bulk crystal at 1186.2 nm, Fig. 8(b), in agreement with Refs. [44,45]. It is also preserved in the spectrum of the epitaxial layer. The intense peaks at 1204.2 and 1210.7 nm which are present in the spectra of both the epitaxial layer and the bulk crystal were assigned by Doroshenko *et al.* to Tm^{3+} clusters [45].

4.4. Judd-Ofelt analysis

The absorption spectrum of the ~6 at.% Tm:CaF_2 film was analyzed using the Judd-Ofelt (J-O) theory [46,47]. The J-O formalism was applied to ED contributions to transition intensities. The contribution of magnetic-dipole (MD) transitions (for $\Delta J = J - J' = 0, \pm 1$, except of $J = J' = 0$) was calculated separately within the Russell–Saunders approximation on wave functions of Tm^{3+} under an assumption of a free-ion. The set of squared reduced matrix elements $U^{(k)}$ was calculated using the free-ion parameters from [48]. The dispersion curve of CaF_2 reported in [16] was used. The details of the calculation can be found elsewhere [49], here, we only discuss the used approximations.

In the standard J-O theory, the ED line strengths of the $J \rightarrow J'$ transitions $S^{ED}(JJ')$ are given by [46,47]:

$$S^{ED}_{calc}(JJ') = \sum_{k=2,4,6} U^{(k)}\Omega_k, \tag{1a}$$

$$U^{(k)} = \langle (4f^n)SLJ \| U^k \| (4f^n)S'L'J' \rangle^2. \tag{1b}$$

Here, $U^{(k)}$ are the reduced squared matrix elements and Ω_k are the intensity (J–O) parameters ($k = 2, 4, 6$).

The standard J-O theory can be modified to account for the configuration interaction. If only the lower-energy excited configuration of the opposite parity ($4f^{n-1}5d^1$) contributes to the configuration interaction, the ED line strengths are [50,51]:

$$S^{ED}_{calc}(JJ') = \sum_{k=2,4,6} U^{(k)}\tilde{\Omega}_k, \tag{2a}$$

$$\tilde{\Omega}_k = \Omega_k[1 + 2\alpha(E_J + E_{J'} - 2E_f^0)]. \tag{2b}$$

Here, the intensity parameters $\tilde{\Omega}_k$ are the linear functions of energies (E_J and $E_{J'}$) of the two multiplets involved in the transition $J \rightarrow J'$, E_f^0 is the mean energy of the $4f^n$ configuration and $\alpha \approx 1/(2\Delta)$, where Δ has the meaning of the average energy difference between the $4f^n$ and $4f^{n-1}5d^1$ electronic configurations. Thus, there are four free parameters, i.e., Ω_2, Ω_4, Ω_6 and α. Note that $\tilde{\Omega}_k$ for the mJ-O theory is transformed into Ω_k in the standard J-O theory under the assumption of a high-lying $4f^{n-1}5d^1$ excited configuration ($\Delta \rightarrow \infty$ or, equivalently, $\alpha \rightarrow 0$).

The measured and calculated absorption oscillator strengths (denoted as f_{exp} and f^{Σ}_{calc}, respectively) are listed in Table 1. Here, the superscript "Σ" stands for the total (ED + MD) value. A comparison of the root-mean-square (r.m.s.) deviations between f_{exp} and f^{Σ}_{calc} indicates that the mJ-O theory provides a much better agreement between the experimental and calculated values. Indeed, the r.m.s. deviation equals to 0.880 (J-O) and 0.369 (mJ-O).

Note that during the calculations, the $^3H_6 \rightarrow {}^3F_4$ transition in absorption was excluded to avoid underestimating the radiative lifetime of the $^3F_4$ state. In our recent study [52], we showed that due to the strong spin-orbit interaction, Tm^{3+} multiplets with the same total angular momentum quantum number J = 4 (i.e., $^3F_4$, $^3H_4$ and $^1G_4$) in certain matrices can form a group of strongly interconnected states. Thus, through the $^1G_4$ excited-state of the $4f^n$ configuration, the effect of excited configurations (e.g., $4f^{n-1}5d^1$) is transferred to the lower-lying states.

The obtained intensity parameters are listed in Table 2. For the mJ-O theory, they are Ω_2 = 3.833, Ω_4 = 1.449 and Ω_6 = 2.569 [10^{-20} cm^2] and α = 0.269 [10^{-4} cm], so that the phenomenological parameter $\Delta = 1.86\times10^4$ cm^{-1}.

The probabilities of radiative spontaneous transitions for individual emission channels $A^{\Sigma}_{calc}(JJ')$ (ED + MD), the luminescence branching ratios $B(JJ')$, the total probabilities of spontaneous radiative transitions from the excited states A_{tot} and the corresponding radiative lifetimes τ_{rad} are listed in Table 3. They are obtained using the mJ-O theory. For the $^3F_4$ and $^3H_4$ Tm^{3+} multiplets, τ_{rad} is 21.30 ms and 1.11 ms, respectively.

4.5. Luminescence spectra

The spectra of RT near-IR luminescence from the Tm:CaF_2 epitaxial layers are shown in Fig. 9(a) (λ_{exc} = 768 nm, excitation to the $^3H_4$ state). For the highly-doped (~6 at.% Tm) layer, an emission band with a maximum at ~1830 nm is observed and assigned to the $^3F_4 \rightarrow {}^3H_6$ transition of Tm^{3+} ions forming clusters. It is smooth and broad (a "glassy"-like behavior), except for two local peaks in the short-wavelength part (at 1613 and 1667 nm). The emission bandwidth (FWHM) $\Delta\lambda_{lum}$ is 182 nm. The shape of this band greatly resembles that for a highly-doped bulk Tm:CaF_2 crystal, Fig. 9(a), but it is broader (for the bulk crystal, $\Delta\lambda_{lum}$ = 144 nm) which implies more complex assemblage of Tm^{3+} species.

For the ~2 at.% Tm-doped film, the emission spectrum is very different. First, the $^3F_4 \rightarrow {}^3H_6$ band is strongly structured exhibiting several prominent peaks at 1700, 1721, 1744, 1768, 1822, 1862 (the most intense) and 1891 nm. Second, another emission band with a maximum at ~1420 nm which also contains a set of well-resolved peaks appears, see Fig. 9(b). It is related to the $^3H_4 \rightarrow {}^3F_4$ Tm^{3+} transition and in the case of Tm:CaF_2, it indicates the presence of isolated ions. In Tm^{3+}-doped materials, there exist an efficient cross-relaxation (CR) process between adjacent Tm^{3+} ions, $^3H_4(Tm_1) + {}^3H_6(Tm_2) \rightarrow {}^3F_4(Tm_1) + {}^3F_4(Tm_2)$, which depopulates the $^3H_4$ state and greatly reduces its luminescence lifetime. Obviously, CR is greatly promoted for Tm^{3+} ions within clusters, so that the emissions from the $^3H_4$ state are very weak even at low Tm doping levels (>0.1 at.%) in bulk CaF_2 crystals [17]. Indeed, the study of a ~1.5 at.% Tm:CaF_2 bulk crystal, Fig. 7(a), reveals no signs of the $^3H_4 \rightarrow {}^3F_4$ emission. It is observed only for the 0.05 at.% Tm-doped bulk crystal. Thus, for the ~2 at.% Tm-doped layer, a significant amount of ions remains isolated. The shapes of the $^3H_4 \rightarrow {}^3F_4$ emission bands for the epitaxial layer and the bulk crystal are rather different suggesting the presence of isolated Tm^{3+} species of different nature in agreement with Section 4.3.

To reveal the nature of Tm^{3+} centers in the epitaxial layers with different doping levels, first, LT luminescence spectra corresponding to the $^3F_4 \rightarrow {}^3H_6$ Tm^{3+} transition were measured

under spectrally-selective excitation, see Fig. 10. In the same figure, for comparison, we have also provided the spectra for bulk 0.05 at.% Tm: and 4.5 at.% Tm:CaF_2 crystals.

For ~2 at.% Tm-doped layer, by scanning the excitation wavelength around 790 nm (the spectral range corresponding to absorption lines of non-identified centers, see Section 4.3), two distinct types of emission spectra were observed, Fig. 10(a), corresponding to λ_{exc} = 792.5 and 793.6 nm. None of them can be assigned to C_{3v} and C_{4v} sites, as evidenced by the measurement performed for the bulk 0.05 at.% Tm:CaF_2 crystal, Fig. 10(b). In Fig. 10(a,b), to simplify the assignment, using known crystal-field splitting of the $^3H_4$ and $^3F_4$ multiplets of Tm^{3+} in the trigonal and tetragonal sites [53,54] and considering the symmetry selection rules [55], we have also calculated the wavelengths of electronic transitions shown by vertical dashes. Thus, we searched for other possible isolated centers. It is known that for CaF_2 crystals, the local charge compensation can be also achieved by oxygen resulting in trigonal oxygen-assisted sites $C_{3v}(T_2)$ [56] appearing instead of the fluorine-compensated C_{3v} ones. The emission spectrum of the ~2 at.% Tm-doped layer observed for λ_{exc} = 793.6 nm is well explained assuming the presence of $C_{3v}(T_2)$ sites.

For the ~6 at.% Tm-doped layer, cf. Fig. 10(c), the LT luminescence spectrum exhibits broad and smooth bands and it is barely sensitive to the excitation wavelength, as shown for the example of λ_{exc} = 762.7 nm. The spectrum also greatly resembles that for the bulk 4.5 at.% Tm:CaF_2 crystal, Fig. 10(d). This type of emission is thus assigned to Tm^{3+} clusters. By tuning the excitation wavelength to λ_{exc} = 793.6 nm, weak signatures of isolated $C_{3v}(T_2)$ sites were detected.

As pointed out above, the $^3H_4 \rightarrow {}^3F_4$ luminescence is very sensitive to the nature of Tm^{3+} emitting centers (i.e., isolated ions or clusters). Thus, it was also studied at low temperature, Fig. 11. No luminescence owing to this transition was observed for the ~6 at.% Tm-doped layer, as expected. For the ~2 at.% Tm-doped layer, λ_{exc} = 793.6 nm leads to intense emission with distinct peaks well explained by electronic transitions of Tm^{3+} ions located in the $C_{3v}(T_2)$ sites (with the wavelengths calculated from the known crystal-field splitting [54] and marked by red dashes), Fig. 11(a). In contrast, for λ_{exc} = 792.5 nm, no emission was observed. The latter suggests that the corresponding centers are not isolated and probably represent small clusters (e.g., dimers) which are different from those observed in the ~6 at.% Tm-doped layer. However, it is difficult to argue if the charge compensation in such small clusters is provided by oxygen or fluorine. No spectroscopic signatures of C_{3v} and C_{4v} sites are found for the ~2 at.% Tm:CaF_2 layer, while both of them are easily found for the bulk 0.05 at.% Tm:CaF_2 crystal, Fig. 11(b).

4.6. Luminescence decay

The RT luminescence decay curves for the Tm:CaF_2 epitaxial layers are shown in Fig. 12 corresponding to emissions from the $^3F_4$ and $^3H_4$ states. In the first experiments with the as-grown films, we observed a "fast" component (characteristic decay time: <100 μs) in the decay curves from the $^3F_4$ state, as shown by the grey curve in Fig. 12(a). However, it was completely eliminated by polishing the top-surface of the films and removing the residual solvent (LiF) and imperfect part of the film. We believe that the "fast" component may represent the effect of defect-assisted sites located near the film surface, small Tm:CaF_2 crystallites formed during the

film cooling, or energy-transfer to defect states in LiF. For the polished ~6 at.% Tm-doped film, the decay from the $^3F_4$ state is well fitted using a single-exponential law yielding the lifetime τ_{lum} = 21.70 ms which is assigned to Tm^{3+} clusters.

The lifetime measurements in Tm^{3+}-doped materials may be affected by reabsorption. To confirm the correctness of our studies, we applied the pinhole method [57] for the ~6 at.% Tm-doped film and did not detect any noticeable variation of τ_{lum} with the pinhole diameter. This can be understood considering the very small thickness of the studied film (t ~ 10 μm).

The luminescence decay from the $^3F_4$ state for the ~2 at.% Tm-doped film is clearly non-single-exponential. When applying a bi-exponential fit, we achieve τ_{lum1} = 4.8±0.5 ms and τ_{lum2} = 24.9±0.7 ms. This observation agrees with our assumption of the multi-site nature of this sample. According to the previous spectrally-selective lifetime measurements performed for bulk Tm:CaF_2 crystals [54], we assign the τ_{lum1} and τ_{lum2} lifetimes to $C_{3v}(T_2)$ and cluster sites, respectively.

The $^3F_4$ lifetimes determined in the present study are longer than those measured for the ~1 at.% Tm:CaF_2 epitaxial film grown using the $CaCl_2$ solvent (τ_{lum} = 12.8 ms, single-exponential fit) [31]. In [31], the lifetime reduction was assigned to quenching effects possibly related to defects and impurities.

As pointed out above, the emissions from the $^3H_4$ Tm^{3+} state in CaF_2 are very sensitive to ion clustering due to cross-relaxation. The decay curves from the $^3H_4$ state for the epitaxial Tm:CaF_2 films are shown in Fig. 12(b) and their shape is characteristic for systems with CR [58,59]. The initial part of the decay curve represents the energy-transfer and the "slow" part which is well fitted with a single-exponential law corresponds to the intrinsic lifetime of the $^3H_4$ state. For the ~2 at.% Tm-doped epitaxy, the intrinsic lifetime τ_{lum0} = 1.26±0.1 ms and the average one $\langle\tau_{lum}\rangle$ = 0.90 ms. For the ~6 at.% Tm-doped film, both values are shorter, namely τ_{lum0} = 0.87±0.05 ms (which is probably due to enhanced energy-migration to defects and impurities) and $\langle\tau_{lum}\rangle$ = 0.175 ms (which is also indicative of enhanced CR). Note that the use of rate-equation formalism for the analysis of decay curves from the $^3H_4$ state as in the previous work [59] is complicated in our case due to the presence of several types of emitting centers (isolated ions and clusters) with their relative ratios being unknown.

4.7. Stimulated-emission cross-sections

The stimulated-emission (SE) cross-sections, σ_{SE}, for the $^3F_4 \rightarrow {}^3H_6$ transition of Tm^{3+} ions in highly-doped film were calculated using the Füchtbauer–Ladenburg (F-L) equation [60]:

$$\sigma_{SE}(\lambda) = \frac{\lambda^5}{8\pi n^2 \tau_{rad} c} \frac{W(\lambda)}{\int \lambda W(\lambda) d\lambda}, \quad (3)$$

where, $W(\lambda)$ is the luminescence spectrum calibrated for the spectral response of the set-up, λ is the light wavelength, n is the refractive index at the mean emission wavelength [16], c is the speed of light, τ_{rad} is the radiative lifetime of the emitting state ($^3F_4$). The results on σ_{SE} for the ~6 at.% Tm-doped layer are shown in Fig. 13(a) and compared with those for a highly-doped bulk crystal. For the epitaxial layer, the maximum σ_{SE} = 0.14×10^{-20} cm^2 at 1856 nm and it is lower than for the corresponding bulk crystal (0.23×10^{-20} cm^2 at 1850 nm). Here, the difference originates mainly from the lifetimes used for the calculation. Physically, the broadening of the

emission band and the reduction of the peak SE cross-sections is due to the more complex assemblage of Tm^{3+} species in the epitaxial layer (e.g., probably slightly different geometry of clusters).

The $^3F_4 \rightarrow {}^3H_6$ Tm^{3+} transition represents a quasi-three level scheme with reabsorption. Thus, the gain cross-sections, $\sigma_g = \beta\sigma_{SE} - (1 - \beta)\sigma_{abs}$, where $\beta = N_2(^3F_4)/N_{Tm}$ is the inversion ratio and N_2 is the population of the upper multiplet, were calculated, Fig. 13(b). The gain spectra are smooth and broad. For small $\beta = 0.10$, the local maximum in the gain spectrum is located at ~1.94 μm. With increasing the inversion ratio, the gain spectrum experiences a blue-shift reaching ~1.86 μm for high $\beta = 0.40$. The determined gain spectra emphasize the advantage of using highly-doped Tm:CaF_2 films for broadband amplification and ultrashort pulse generation in waveguide geometry.

4.8. Isolated ions: discussion

Oxygen-assisted sites. In our previous study of 1.4 at.% Yb:CaF_2 epitaxial layers grown using another solvent ($CaCl_2$), it was evidenced that a significant fraction of Yb^{3+} ions is located in isolated sites [22]. The assemblage of Yb^{3+} species was as following: isolated sites ($C_{3v}(T_2)$ - predominantly, O_h – well-detected and C_{4v} – minor fraction) and clusters. This agrees with the present work.

We relate the presence of oxygen in the films to the possible weak pollution of the molten bath with residual moisture and / or oxygen traces in the growth chamber, despite a special attention was paid to reach a good secondary vacuum before starting the molten ramp of the precursors. Fluorides in the molten state are very sensitive to oxygen pollution. For the technical point of view, we cannot exclude the infiltration of air through the seals of the pulling cane by dint of repeated translations or due to many openings of the exchange airlock to change and install samples at the extremity of the cane, despite the systematic pumping and Ar-refilling of the charging dock. The LPE run is typically done during few weeks comprising multiple samples.

Cubic sites. The presence of cubic sites in even highly-doped Tm:CaF_2 films is not surprising. Petit *et al.* indicated that in bulk Yb:CaF_2 crystals, the relative fraction of isolated ions residing in O_h sites is barely sensitive to the doping concentration (in the range of 0.03-0.12 at.%) as compared to those for the C_{3v} and C_{4v} sites whose relative occupations decrease at the expense of cluster formation [42]. A similar conclusion was made in [61] for bulk CaF_2 doped with 0.01-0.2 mol% Er.

It is also known that univalent alkali metals (Na^+, Li^+, K^+) may enter into the CaF_2 lattice [62]. They can be intentionally introduced in the form of the NaF, LiF or KF reagents [63] or may come as impurities. The sites formed by the Tm^{3+} and Na^+ cations exhibit C_{2v} symmetry. In addition, Tm^{3+} ions in Na-codoped CaF_2 crystals can reside in cubic sites (O_h) with a non-local charge compensation, however, the symmetry of these cubic sites is disturbed by neighboring Na^+ cations. It was found that the alkali metal codoping of CaF_2 promotes the formation of cubic sites for rare-earth dopants [62].

In analogy to Na^+ codoping of Tm:CaF_2, one may suggest the presence of Li^+ in the grown films. Bulk Tm,Li:CaF_2 crystals were grown [62]. However, due to a large difference of ionic

radii of Ca^{2+} and Li^{+} (as compared to Na^{+}), the segregation of Li^{+} in CaF_2 is very low. Nevertheless, we cannot exclude that a certain (small) amount of Li is present in our films, especially since LiF has been used as a solvent. The EDX analysis did not allow to detect lithium due to its too low atomic number.

Isolated ions vs. clusters. To summarize, our studies indicate that with the Tm doping of epitaxial CaF_2 films, the probability of cluster formation increases, but this tendency is much slower than in in the case of bulk crystals. As a result, a significant fraction of isolated ions is present in ~2 at.% Tm-doped films and isolated ions are still found in ~6 at.% Tm-doped films. The site symmetries for the isolated ions are identified as $C_{3v}(T_2)$ and O_h.

A similar tendency for "slow" clustering was observed previously in rare-earth doped CaF_2 films grown by MBE. Daran *et al*. studied films doped with Er and indicated that the relative fraction of ions in C_{4v} sites with respect to those forming clusters decreases rapidly with the doping level; almost no isolated ions were found at ~6 mol% Er doping [64]. The authors pointed out that this process is slowed down as compared to bulk crystals for which a similar effect already occurred at ~1 mol% Er [64]. Bausa *et al*. studied Nd-doped CaF_2 films and concluded that the lower growth temperature in the case of MBE greatly affects the formation of clusters involving several Nd^{3+} - F- pairs [65]. This was assigned to solid-state diffusion which is slowed down with reducing the temperature: Osiko *et al*. indicated that the impurity complexes become virtually immobile at the temperatures below 600 °C [66]. Moreover, it was stated that for a given doping concentration, the distribution of ions over different types of sites (both isolated or clusters) is different for epitaxial films and bulk crystals [65]. This agrees with our observations.

The authors of [67] indicated that the assemblage of rare-earth species in CaF_2 depends on the thermodynamic equilibrium conditions during the growth of the films or bulk crystals. Drazic *et al*. indicated that the degree of inhomogeneous distribution of Tm^{3+} ions in bulk CaF_2 and ion clustering depend on (i) the heat flow gradients across the interface between the melt and solid phases, (ii) the temperature gradient in the crucible and (iii) the spatial correlation between the density fluctuations in the liquid phase. The growth temperatures for the studied LPE films T = 815 – 856 °C are significantly lower than the growth temperature of bulk Tm:CaF_2 which lies around 1418 °C. The vertical thermal gradients in the crucible during the LPE growth were estimated as 0.5 – 1 °C/cm, whereas they are about ~40 °C/cm in the case of bulk CaF_2 crystals grown by the Bridgman technique. The different thermodynamic conditions during the LPE growth and the bulk crystal growth and, in particular, much lower growth temperature in the former case, can also explain the notable difference of segregation coefficients of rare-earth ions in these two forms of CaF_2 (K_{Tm} is near unity for bulk crystals and almost twice smaller for LPE films).

4.9. Waveguiding properties

It is known that rare-earth doping of CaF_2 enhances its refractive index. Thus, Tm:CaF_2 / CaF_2 epitaxies can serve as optical waveguides (in planar geometry). To verify this, we studied a ~2 at.% Tm-doped epitaxy. Its top surface was polished to laser quality resulting in a film thickness of 36±1 μm. The input and output facets were also polished with good parallelism

and the length of the sample was 5.0 mm. Figure 14 shows the near-field profile of the guided mode at 770 nm at the output facet of the epitaxy. The mode has a characteristic horizontal stripe profile typical for planar waveguides. The variation of the refractive index in the ~2 at.% Tm-doped epitaxy, $\Delta n = n_{layer} - n_{substrate}$, was estimated to be 0.008 ($n_{substrate}$ = 1.432) at the wavelength of 632.8 nm, using the data from [31].

A rough upper estimation for waveguide propagation losses was obtained from the pump-transmission measurements at ~850 nm (out of Tm^{3+} absorption), $\delta_{loss} < 1$ dB/cm. The precision was limited by the relatively short epitaxial sample. In [22] for a similar 1.4 at.% Yb:CaF_2 epitaxy, δ_{loss} was estimated with higher precision from the Findlay-Clay analysis of the laser performance to be as low as 0.14±0.05 dB/cm at ~1 μm.

5. Conclusions

The spectroscopic study of Tm^{3+}-doped CaF_2 layers grown by LPE allowed us to draw the following conclusions:

(i) The predominant type of sites for isolated Tm^{3+} ions in the epitaxial films is the oxygen-assisted trigonal site $C_{3v}(T_2)$. No spectroscopic signatures of fluorine-compensated C_{3v} and C_{4v} sites are found in the films doped with ~2 at.% Tm while a certain fraction of ions reside in cubic sites (O_h) which are preserved even at high doping levels (~6 at.% Tm).

(ii) With increasing the doping level, Tm^{3+} ions tend to form clusters with optical properties similar to those in bulk Tm:CaF_2 crystals. Highly-doped Tm:CaF_2 films contain predominantly clusters leading to smooth and broad spectral bands (a "glassy-like" behavior) and a nearly single-exponential decay from the upper laser level ($^3F_4$) with a lifetime of 21.70 ms which is well explained by the Judd-Ofelt theory.

(iii) The formation of Tm clusters in the epitaxial films with their doping is slowed down as compared to the corresponding single crystals. This is explained by the different thermodynamic growth conditions for the epitaxial layers and bulk crystals, and, in particular, by much lower growth temperature for the LPE method (T = 815 – 856 °C, in the present work) slowing down the solid-state diffusion of defects serving for charge compensation (e.g., interstitial fluorine, F_i^- and / or oxygen O^{2-}). As a result, a significant part of Tm^{3+} ions in ~2 at.% Tm-doped films is located in isolated sites which has a direct consequence on the emission properties. Even for ~6 at.% Tm-doped films, the spectroscopic signatures of ions in $C_{3v}(T_2)$ and O_h sites can still be found.

The detailed morphological study of the films allowed us to conclude that Tm^{3+}-doped CaF_2 layers grown on (100) oriented substrates are prone to crazing forming a characteristic rectangular pattern of cracks oriented along the [011] and [01$\bar{1}$] directions. This effect seems to be promoted by Tm doping. It can be greatly reduced by a proper temperature regime of the epitaxial growth. One may argue that such micro-cracks or even dislocations that are not directly visible as cracks increase the waveguide propagation losses of the films, so that the elimination of crazing is crucial. As pointed out above, it can be reached by a proper (e.g., two-step) temperature regime or by using other substrate orientations, e.g., (111) or non-oriented ones.

Highly-doped Tm:CaF_2 films with predominantly clustered Tm^{3+} ions, because of their smooth and broad emission spectra of the $^3F_4 \rightarrow {}^3H_6$ transition, efficient cross-relaxation between adjacent Tm^{3+} ions and long upper laser lifetime are promising for waveguide laser applications at ~2 μm.

Acknowledgements

This work was supported by French Agence Nationale de la Recherche (ANR) through the projects LabEx EMC3 (ANR-10-LABX-09-01), SPLENDID2 (ANR-19-CE08-0028), and the European project "NOVAMAT" co-funded by the European Community funds FEDER and the Normandie region.

References

1. P. Camy, J.L. Doualan, S. Renard, A. Braud, V. Menard, R. Moncorgé, Tm^{3+}:CaF_2 for 1.9 μm laser operation, Opt. Commun. 236 (2004) 395-402.
2. R. C. Stoneman, L. Esterowitz, Efficient, broadly tunable, laser-pumped Tm:YAG and Tm:YSGG cw lasers, Opt. Lett. 15 (1990) 486-488.
3. Y. Wang, W. Chen, M. Mero, L. Zhang, H. Lin, Z. Lin, G. Zhang, F. Rotermund, Y. J. Cho, P. Loiko, X. Mateos, U. Griebner, V. Petrov, Sub-100 fs Tm:$MgWO_4$ laser at 2017 nm mode locked by a graphene saturable absorber, Opt. Lett. 42 (2017) 3076-3079.
4. M. Schellhorn, High-power diode-pumped Tm: YLF laser, Appl. Phys. B 91 (2008) 71-74.
5. K. van Dalfsen, S. Aravazhi, C. Grivas, S. M. García-Blanco, M. Pollnau, Thulium channel waveguide laser with 1.6 W of output power and ~80% slope efficiency, Opt. Lett. 39 (2014) 4380-4383.
6. A. Rameix, C. Borel, B. Chambaz, B. Ferrand, D. P. Shepherd, T. J. Warburton, D. C. Hanna, A. C. Tropper, An efficient, diode-pumped, 2 μm Tm:YAG waveguide laser, Opt. Commun. 142 (1997) 239–243.
7. W. Bolanos, F. Starecki, A. Benayad, G. Brasse, V. Ménard, J.-L. Doualan, A. Braud, R. Moncorgé, P. Camy, Tm:$LiYF_4$ planar waveguide laser at 1.9 μm, Opt. Lett. 37 (2012) 4032–4034.
8. W. Bolaños, J. J. Carvajal, X. Mateos, E. Cantelar, G. Lifante, U. Griebner, V. Petrov, V. L. Panyutin, G. S. Murugan, J. S. Wilkinson, M. Aguiló, F. Díaz, Continuous-wave and Q-switched Tm-doped $KY(WO_4)_2$ planar waveguide laser at 1.84 μm, Opt. Express 19 (2011) 1449–1454.
9. K. van Dalfsen, S. Aravazhi, D. Geskus, K. Wörhoff, M. Pollnau, Efficient $KY_{1-x-y}Gd_xLu_y(WO_4)_2$:$Tm^{3+}$ channel waveguide lasers, Opt. Express 19 (2011) 5277–5282.
10. P. Loiko, R. Soulard, G. Brasse, J.-L. Doualan, B. Guichardaz, A. Braud, A. Tyazhev, A. Hideur, P. Camy, Watt-level Tm:$LiYF_4$ channel waveguide laser produced by diamond saw dicing, Opt. Express 26 (2018) 24653-24662.
11. P. Loiko, J. M. Serres, X. Mateos, S. Tacchini, M. Tonelli, S. Veronesi, D. Parisi, A. Di Lieto, K. Yumashev, U. Griebner, V. Petrov, Comparative spectroscopic and thermo-optic study of Tm:$LiLnF_4$ (Ln = Y, Gd, and Lu) crystals for highly-efficient microchip lasers at ~2 μm, Opt. Mater. Express 7 (2017) 844-854.
12. M. Chen, P. Loiko, J. M. Serres, S. Veronesi, M. Tonelli, M. Aguiló, F. Díaz, J. E. Bae, T. G. Park, F. Rotermund, S. Dai, Z. Chen, U. Griebner, V. Petrov, X. Mateos, Fluorite-type Tm^{3+}:KY_3F_{10}: A promising crystal for watt-level lasers at ~1.9 μm, J. Alloys Compd. 813 (2020) 152176-1-8.
13. F. Cornacchia, D. Parisi, C. Bernardini, A. Toncelli, M. Tonelli, Efficient, diode-pumped Tm^{3+}:BaY_2F_8 vibronic laser, Opt. Express 12 (2004) 1982-1989.

14. A. Sottile, E. Damiano, M. Rabe, R. Bertram, D. Klimm, M. Tonelli, Widely tunable, efficient 2 μm laser in monocrystalline Tm^{3+}:SrF_2, Opt. Express 26 (2018) 5368-5380.
15. G. A. Slack, Thermal conductivity of CaF_2, MnF_2, CoF_2, and ZnF_2 crystals, Phys. Rev. 122 (1961) 1451.
16. I. H. Malitson, A redetermination of some optical properties of calcium fluoride, Appl. Opt. 2 (1963) 1103-1107.
17. S. Renard, P. Camy, A. Braud, J.L. Doualan, R. Moncorgé, CaF_2 doped with Tm^{3+}: A cluster model, J. Alloys Compd 451 (2008) 71-73.
18. J. Liu, C. Zhang, Z. Zhang, J. Wang, X. Fan, J. Liu, L. Su, 1886-nm mode-locked and wavelength tunable Tm-doped CaF_2 lasers, Opt. Lett. 44, 134-137 (2019).
19. Z. Zhang, X. Guo, J. Wang, C. Zhang, J. Liu, L. Su, High-efficiency 2 μm continuous-wave laser in laser diode-pumped Tm^{3+}, La^{3+}:CaF_2 single crystal, Opt. Lett. 43 (2018) 4300-4303.
20. K. Nassau, Application of the Czochralski method to divalent metal fluorides, J. Appl. Phys. 32 (1961) 1820-1821.
21. L.E. Bausa, G. Lifante, E. Daran, P.L. Pernas, CaF_2:Er^{3+} molecular beam epitaxial layers as optical waveguides, Appl. Phys. Lett. 68 (1996), 3242-3244.
22. P. Loiko, R. Soulard, E. Kifle, L. Guillemot, G. Brasse, A. Benayad, J.-L. Doualan, A. Braud, M. Aguiló, F. Díaz, X. Mateos, P. Camy, Ytterbium calcium fluoride waveguide laser, Opt. Express 27 (2019) 12647-12658.
23. L.J. Schowalter, R.W. Fathauer, R.P. Goehner, L.G. Turner, R.W. DeBlois, S. Hashimoto, J.L. Peng, W.M. Gibson, J.P. Krusius, Epitaxial growth and characterization of CaF_2 on Si, J. Appl. Phys. 58 (1985) 302-308.
24. R.W. Fathauer, L.J. Schowalter, Surface morphology of epitaxial CaF_2 films on Si substrates, Appl. Phys. Lett. 45 (1984) 519-521.
25. S. Sinharoy, R.A. Hoffman, J.H. Rieger, R.F.C. Farrow, A.J. Noreika, Epitaxial growth of CaF_2 on GaAs (100), J. Vac. Sci. Technol. A, 3 (1985) 842-845.
26. E. Daran, L.E. Bausa, A. Muñoz-Yagüe, C. Fontaine, Er^{3+} doping of CaF_2 layers grown by molecular beam epitaxy, Appl. Phys. Lett. 62 (1993) 2616-2618.
27. F. Lahoz, E. Daran, G. Lifante, T. Balaji, A. Muñoz-Yagüe, CaF_2:Yb^{3+}+Pr^{3+} codoped waveguides grown by molecular beam epitaxy for 1.3 μm applications, Appl. Phys. Lett. 74 (1999) 1060-1062.
28. T. Balaji, G. Lifante, E. Daran, R. Legros, G. Lacoste, Growth by molecular beam epitaxy and characterization of CaF_2:Pr^{3+} planar waveguides, Thin Solid Films 339 (1999) 187-193.
29. L.E. Bausa, R. Legros, A. Muñoz-Yagüe, Nd^{3+} incorporation in CaF_2 layers grown by molecular beam epitaxy, Appl. Phys. Lett. 59 (1991) 152-154.
30. A. Peña, P. Camy, A. Benayad, J.-L. Doualan, C. Maurel, M. Olivier, V. Nazabal, R. Moncorgé, Yb:CaF_2 grown by liquid phase epitaxy, Opt. Mater. 33 (2011) 1616-1620.
31. S. Renard, P. Camy, J. L. Doualan, R. Moncorgé, M. Couchaud, B. Ferrand, Tm^{3+}: CaF_2 planar waveguides grown by liquid phase epitaxy on CaF_2 substrates showing signal enhancement at 1.92 μm, Opt. Mater. 28 (2006) 1289-1291.
32. G. Brasse, P. Loiko, C. Grygiel, P. Leprince, A. Benayad, F. Lemarie, J.L. Doualan, A. Braud, P. Camy, Liquid Phase Epitaxy growth of Tm^{3+}-doped CaF_2 thin-films based on LiF solvent, J. Alloy Compd. 803 (2019) 442-449.
33. R. Soulard, M. Salhi, G. Brasse, P. Loiko, J.-L. Doualan, L. Guillemot, A. Braud, A. Tyazhev, A. Hideur, P. Camy, Laser operation of highly-doped Tm:$LiYF_4$ epitaxies: towards thin-disk lasers, Opt. Express 27 (2019) 9287-9301.

34. P.W. Sullivan, R.F.C. Farrow, G.R. Jones, Insulating epitaxial films of BaF_2, CaF_2 and $Ba_xCa_{1-x}F_2$ grown by MBE on InP substrates, J. Cryst. Growth 60 (1982) 403-413.
35. S. Siskos, C. Fontaine, A. Munoz-Yague, Epitaxial growth of lattice-matched $Ca_xSr_{1-x}F_2$ on (100) and (110) GaAs substrates, J. Appl. Phys. 56 (1984) 1642-1646.
36. T. Minemura, J. Asano, K. Tsutsui, S. Furukawa, Influence of off-oriented substrates on the crystallinity of $(Ca,Sr)F_2$ layers grown on Si (100), Appl. Phys. Lett. 56 (1990) 2198-2200.
37. J.P. Russell, The Raman spectrum of calcium fluoride, Proc. Phys. Soc. 85 (1965) 194.
38. M. Mujaji, J.D. Comins, A Raman study of the superionic behaviour of CaF_2 crystals containing trivalent lanthanide ions, Phys. Status Solidi C 4 (2007) 851-855.
39. A.R. Gee, D.C. O'Shea, H.Z. Cummins, Raman scattering and fluorescence in calcium fluoride, Solid State Commun. 4 (1966) 43-46.
40. A.R. Evans, D.B. Fitchen, Raman spectra of alkali fluoride crystals, Solid State Commun. 8 (1970) 537-539.
41. K.P. Jain, S. Radhakrishna, A.K. Prabhakaran, Raman-scattering studies in LiF crystals containing manganese, Phys. Rev. B 5 (1972) 2325-2328.
42. V. Petit, P. Camy, J.L. Doualan, X. Portier, R. Moncorgé, Spectroscopy of Yb^{3+}:CaF_2: From isolated centers to clusters, Phys. Rev. B 78 (2008) 085131.
43. B. Lacroix, C. Genevois, J.L. Doualan, G. Brasse, A. Braud, P. Ruterana, P. Camy, E. Talbot, R. Moncorgé, J. Margerie, Direct imaging of rare-earth ion clusters in Yb:CaF_2, Phys. Rev. B 90 (2014) 125124.
44. N.M. Strickland, G.D. Jones, Site-selective spectroscopy of Tm^{3+} centers in CaF_2:Tm^{3+}, Phys. Rev. B 56 (1997) 10916-10929.
45. M.E. Doroshenko, K.A. Pierpoint, O.K. Alimov, A.G. Papashvili, V.A. Konyushkin, A.N. Nakladov, Formation of Tm-Y centers in CaF_2-YF_3:Tm^{3+} solid-solution crystals, J. Lumin. 208 (2019) 475-478.
46. B.R. Judd, Optical absorption intensities of rare-earth ions, Phys. Rev. 127 (1962) 750–761.
47. G.S. Ofelt, Intensities of crystal spectra of rare-earth ions, J. Chem. Phys. 37 (1962) 511–520.
48. P.S. Peijzel, P. Vergeer, A. Meijerink, M.F. Reid, L.A. Boatner, G.W. Burdick, $4f^{n-1}5d \rightarrow 4f^n$ emission of Ce^{3+}, Pr^{3+}, Nd^{3+}, Er^{3+}, and Tm^{3+} in $LiYF_4$ and YPO_4, Phys. Rev. B 71 (2005) 045116-1-9.
49. L. Zhang, H. Lin, G. Zhang, X. Mateos, J. M. Serres, M. Aguiló, F. Díaz, U. Griebner, V. Petrov, Y. Wang, P. Loiko, E. Vilejshikova, K. Yumashev, Z. Lin, W. Chen, Crystal growth, optical spectroscopy and laser action of Tm^{3+}-doped monoclinic magnesium tungstate, Opt. Express 25 (2017) 3682-3693.
50. A.A. Kornienko, A.A. Kaminskii, E.B. Dunina, Dependence of the line strength of f–f transitions on the manifold energy. II. Analysis of Pr^{3+} in $KPrP_4O_{12}$, Phys. Status Solidi B 157 (1990) 267-273.
51. P. Loiko, A. Volokitina, X. Mateos, E. Dunina, A. Kornienko, E. Vilejshikova, M. Aguilo, F. Diaz, Spectroscopy of Tb^{3+} ions in monoclinic $KLu(WO_4)_2$ crystal: application of an intermediate configuration interaction theory, Opt. Mater. 78 (2018) 495-501.
52. F. Yue, P. Loiko, M. Chen, J.M. Serres, Y. Wang, J. Li, L. Basyrova, E. Dunina, A. Kornienko, L. Fomicheva, S. Dai, Z. Chen, J.E. Bae, T.G. Park, F. Rotermund, V. Jambunathan, A. Lucianetti, T. Mocek, M. Aguiló, F. Díaz, U. Griebner, V. Petrov, X. Mateos, Spectroscopy and diode-pumped laser operation of transparent Tm:$Lu_3Al_5O_{12}$ ceramics produced by solid-state sintering, Opt. Express 28 (2020) 28399-28413.
53. N.M. Strickland, G.D. Jones, Site-selective spectroscopy of Tm^{3+} centers in CaF_2:Tm^{3+}, Phys. Rev. B 56 (1997) 10916-10929.

54. S. Renard, Synthèse, spectroscopie sélective et fonctionnement laser de CaF_2 : Tm^{3+} sous forme massive et en couches minces, PhD thesis, Universite de Caen, 2005.
55. F.A. Cotton, Chemical applications of group theory, 3rd Ed., Wiley, New York, 1963.
56. M. L. Falin, K. I. Gerasimov, V. A. Latypov, A. M. Leushin, H. Bill, D. Lovy, EPR and optical spectroscopy of Yb^{3+} ions in CaF_2 and SrF_2," J. Lumin. 102–103 (2003) 239–242.
57. H. Kühn, S. T. Fredrich-Thornton, C. Kränkel, R. Peters, K. Petermann, Model for the calculation of radiation trapping and description of the pinhole method, Opt. Lett. 32 (2007) 1908–1910.
58. P. Loiko, M. Pollnau, Stochastic model of energy-transfer processes among rare-earth ions. Example of Al_2O_3:Tm^{3+}, J. Phys. Chem. C 20 (2016) 26480-26489.
59. A. Albalawi, S. Varas, A. Chiasera, H. Gebavi, W. Albalawi, W. Blanc, R. Balda, A. Lukowiak, M. Ferrari, S. Taccheo, Determination of reverse cross-relaxation process constant in Tm-doped glass by $^3H_4$ fluorescence decay tail fitting, Opt. Mater. Express 7 (2017) 3760-3768.
60. B. F. Aull, H. P. Jenssen, Vibronic interactions in Nd:YAG resulting in nonreciprocity of absorption and stimulated emission cross sections, IEEE J. Quantum Electron. 18 (1982) 925-930.
61. D.S. Moore, J.C. Wright, Laser spectroscopy of defect chemistry in CaF_2:Er^{3+}, J. Chem. Phys. 74 (1981) 1626-1636.
62. G.D. Jones, R.J. Reeves, Na^+, Li^+ and cubic centres in rare-earth-doped CaF_2 and SrF_2, J. Lumin. 87 (2000) 1108-1111.
63. L. Su, J. Xu, H. Li, L. Wen, Y. Zhu, Z. Zhao, Y. Dong, G. Zhou, J. Si, Sites structure and spectroscopic properties of Yb-doped and Yb,Na-codoped CaF_2 laser crystals, Chem. Phys. Lett. 406 (2005) 254-258.
64. E. Daran, R. Legros, A. Muñoz-Yagüe, C. Fontaine, L.E. Bausá, Effect of growth temperature and doping concentration on the distribution of the emitting centers in CaF_2:Er molecular beam epitaxial layers, J. Appl. Phys. 75 (1994) 2749-2752.
65. L.E. Bausa, R. Legros, A. Muñoz-Yagüe, Effect of Nd^{3+} concentration on the emission spectra of CaF_2:Nd layers grown by molecular-beam epitaxy, J. Appl. Phys. 70 (1991) 4485-4489.
66. V. V. Osiko, I. A. Shcherbakov, Calculation of point-defect equilibrium in CaF_2-NdF_3 crystals, Sov. Phys. Solid State 14 (1971) 820.
67. G. Dražić, S. Kobe, A.C. Cefalas, E. Sarantopoulou, Z. Kollia, Observation of nanostructured cluster formation of Tm ions in CaF_2 crystals, Mater. Sci. Eng. B 152 (2008) 119-124.

List of figure captions

Figure 1. Scanning Electron Microscope (SEM) images of the LPE-grown ~6 at.% Tm:CaF_2 film (top view): (a-c) raw (as-grown) film surface observed with different magnifications, (d) crazing of polished film.

Figure 2. Scanning Electron Microscope (SEM) image of the side surface of the ~6 at.% Tm:CaF_2 / CaF_2 epitaxy.

Figure 3. (a) Element distribution across the end-facet of the ~6 at.% Tm:CaF_2 / CaF_2 epitaxy analyzed by EDX spectroscopy. All profiles are normalized to unity and shifted along the vertical axis; (b) EDX mapping of Tm.

Figure 4. Confocal laser microscope study of the ~6 at.% Tm:CaF_2/CaF_2 epitaxy: (a,b) top view: (a) raw surface after removing the residual solvent, (b) polished surface; (c,d): side view: (c) without polarizers, (d) in crossed polarizers. Transmission mode, λ = 405 nm.

Figure 5. Unpolarized RT μ-Raman spectra measured from the top (raw, as-grown) and side (polished) surfaces of the ~6 at.% Tm:CaF_2/CaF_2 epitaxy, *numbers* denote the Raman frequencies in cm^{-1}, *asterisks* mark the peaks due to the Tm^{3+} luminescence, λ_{exc} = 488.0 nm. The spectrum for LiF is given for comparison.

Figure 6. RT absorption of Tm^{3+} ions in LPE-grown Tm:CaF_2 thin-films: (a) an overview absorption spectrum for a ~6 at.% Tm-doped film; (b,c) absorption cross-sections, σ_{abs}, for the (b) $^3H_6 \rightarrow {}^3H_4$ and (c) $^3H_6 \rightarrow {}^3F_4$ transitions of Tm^{3+} ions; the spectra for bulk Tm:CaF_2 crystals are given for comparison.

Figure 7. RT excitation spectra for the LPE-grown Tm:CaF_2 thin-films, the spectra for bulk crystals are given for comparison, λ_{lum} = 1810 nm.

Figure 8. LT (12 K) absorption spectra of LPE-grown ~6 at.% Tm:CaF_2 thin-films, the spectra for bulk 1.5 at.% Tm:CaF_2 crystal are given for comparison. Transitions: (a) $^3H_6 \rightarrow {}^3F_4$, (b) $^3H_6 \rightarrow {}^3H_5$, (c) $^3H_6 \rightarrow {}^3H_4$ and (d) $^3H_6 \rightarrow {}^3F_{2,3}$. O^{2-} mark peaks assigned to oxygen-assisted sites (after [54]), O_h – to cubic sites.

Figure 9. Near-IR RT luminescence of Tm^{3+} ions in LPE-grown Tm:CaF_2 thin-films: (a) overview spectra for the ~2 at.% and ~6 at.% Tm:CaF_2 layers, the spectra for bulk crystals are given for comparison; (b) a close look at the $^3H_4 \rightarrow {}^3F_4$ emission for the ~2 at.% Tm:CaF_2 layer. λ_{exc} = 768 nm.

Figure 10. LT (12 K) luminescence spectra of Tm:CaF_2 epitaxial layers and bulk crystals corresponding to the $^3F_4 \rightarrow {}^3H_6$ Tm^{3+} transition measured under spectrally-selective excitation: (a) epitaxy, ~2 at.% Tm, (b) bulk crystal, 0.05 at.% Tm, (c) epitaxy, ~6 at% Tm and (d) bulk crystal, 4.5 at.% Tm. *Grey curves* – RT emission spectra (measured under non-selective excitation), *vertical dashes* – theoretical positions of electronic transitions for Tm^{3+} ions in C_{3v}, C_{4v} and $C_{3v}(T_2)$ sites in CaF_2.

Figure 11. LT (12 K) luminescence spectra of (a) ~2 at.% Tm:CaF_2 epitaxial layer and (b) 0.05 at.% Tm:CaF_2 bulk crystal corresponding to the $^3H_4 \rightarrow {}^3F_4$ Tm^{3+} transition measured under spectrally-selective excitation. *Grey curves* – RT emission spectra (measured under non-selective excitation), *vertical dashes* – theoretical positions of electronic transitions for Tm^{3+} ions in C_{3v}, C_{4v} and $C_{3v}(T_2)$ sites in CaF_2.

Figure 12. RT luminescence decay curves for LPE-grown polished Tm:CaF_2 thin-films: (a) emission from the $^3F_4$ state, λ_{lum} = 1830 nm; (c,d) emission from the $^3H_4$ state, λ_{lum} = 809 nm. λ_{exc} = 765 nm. In (a), the decay curve measured from the raw (as-grown) surface of the epitaxy is shown for comparison.

Figure 13. RT emission properties of Tm^{3+} ions in LPE-grown ~6 at.% Tm:CaF_2 thin-films: (a) stimulated-emission cross-sections, σ_{SE}, for the $^3F_4 \rightarrow {}^3H_6$ transition; the spectrum for bulk crystal is given for comparison; (b) gain cross-section, $\sigma_g = \beta\sigma_{SE} - (1 - \beta)\sigma_{abs}$, spectra for various inversion ratios $\beta = N_2(^3F_4)/N_{Tm}$.

Figure 14. Near-field profile of the guided pump mode at 770 nm for the Tm:CaF_2 / CaF_2 epitaxy, *white lines* mark layer / substrate and layer / air interfaces.

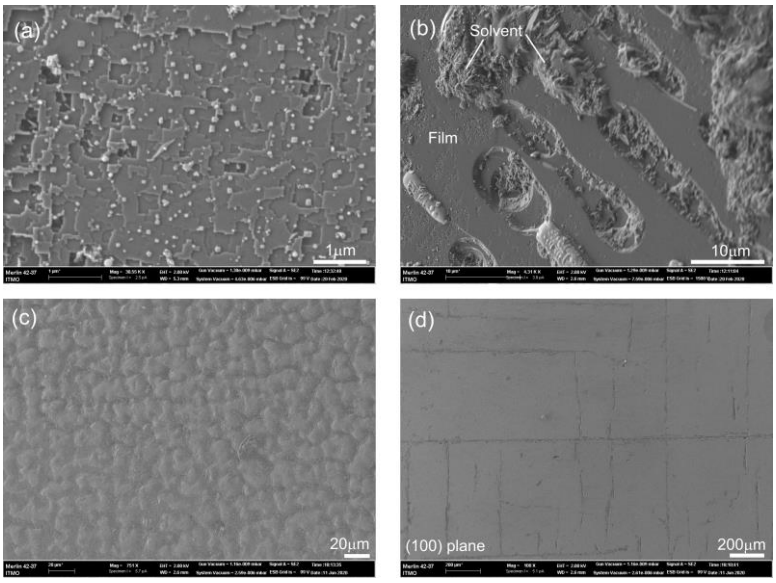

Figure 1. Scanning Electron Microscope (SEM) images of the LPE-grown ~6 at.% Tm:CaF_2 film (top view): (a-c) raw (as-grown) film surface observed with different magnifications, (d) crazing of polished film.

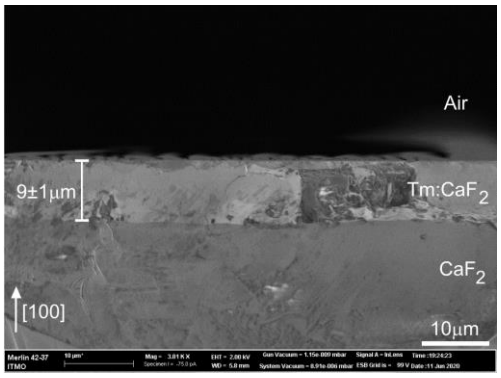

Figure 2. Scanning Electron Microscope (SEM) image of the side surface of the ~6 at.% Tm:CaF_2 / CaF_2 epitaxy.

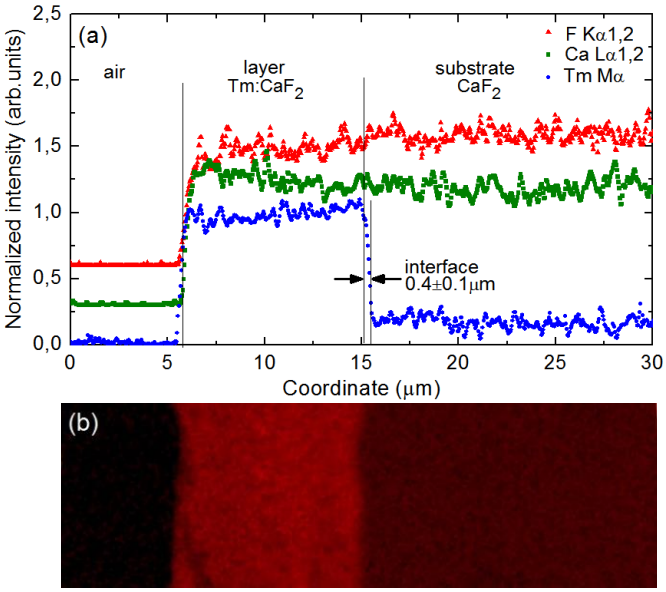

Figure 3. (a) Element distribution across the end-facet of the ~6 at.% Tm:CaF_2 / CaF_2 epitaxy analyzed by EDX spectroscopy. All profiles are normalized to unity and shifted along the vertical axis; (b) EDX mapping of Tm.

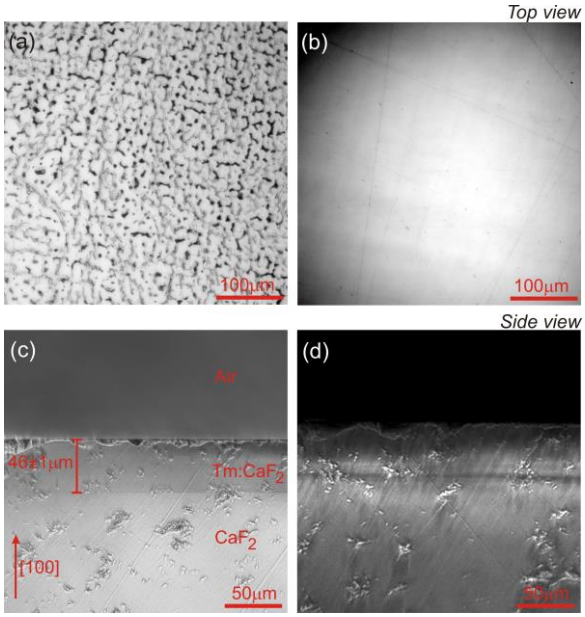

Figure 4. Confocal laser microscope study of the ~6 at.% Tm:CaF_2/CaF_2 epitaxy: (a,b) top view: (a) raw surface after removing the residual solvent, (b) polished surface; (c,d): side view: (c) without polarizers, (d) in crossed polarizers. Transmission mode, λ = 405 nm.

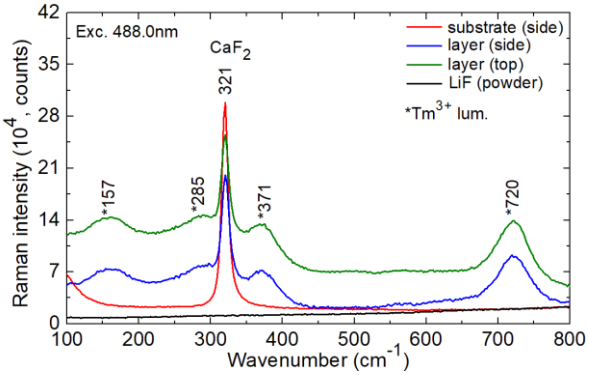

Figure 5. Unpolarized RT μ-Raman spectra measured from the top (raw, as-grown) and side (polished) surfaces of the ~6 at.% Tm:CaF_2/CaF_2 epitaxy, *numbers* denote the Raman frequencies in cm^{-1}, *asterisks* mark the peaks due to the Tm^{3+} luminescence, λ_{exc} = 488.0 nm. The spectrum for LiF is given for comparison.

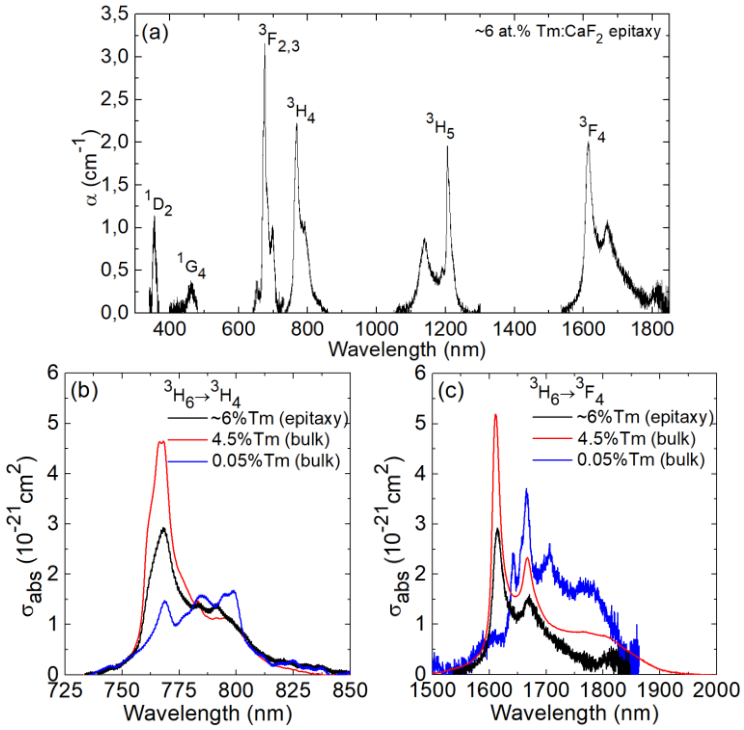

Figure 6. RT absorption of Tm^{3+} ions in LPE-grown Tm:CaF_2 thin-films: (a) an overview absorption spectrum for a ~6 at.% Tm-doped film; (b,c) absorption cross-sections, σ_{abs}, for the (b) $^3H_6 \rightarrow {}^3H_4$ and (c) $^3H_6 \rightarrow {}^3F_4$ transitions of Tm^{3+} ions; the spectra for bulk Tm:CaF_2 crystals are given for comparison.

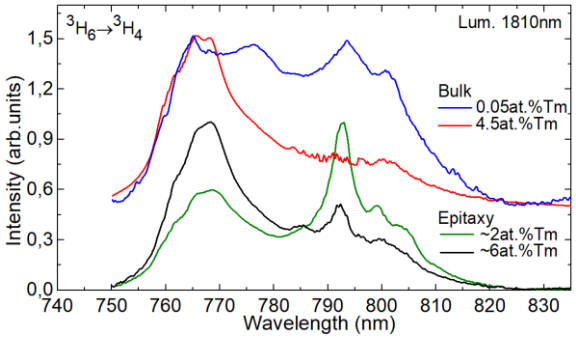

Figure 7. RT excitation spectra for the LPE-grown Tm:CaF_2 thin-films, the spectra for bulk crystals are given for comparison, λ_{lum} = 1810 nm.

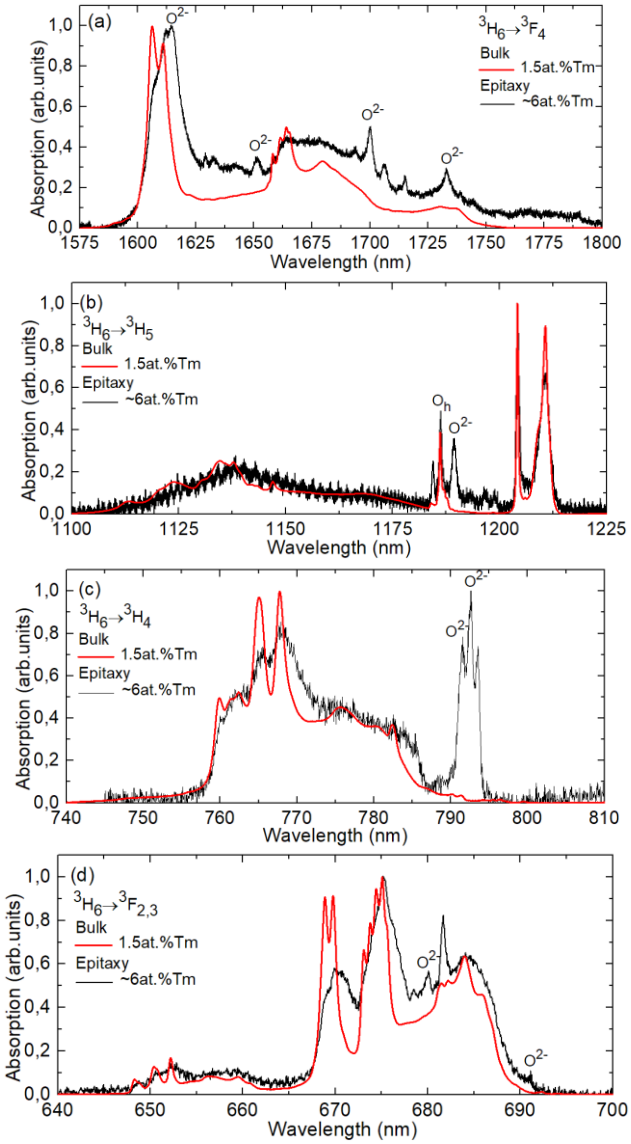

Figure 8. LT (12 K) absorption spectra of LPE-grown ~6 at.% Tm:CaF_2 thin-films, the spectra for bulk 1.5 at.% Tm:CaF_2 crystal are given for comparison. Transitions: (a) $^3H_6 \rightarrow {}^3F_4$, (b) $^3H_6 \rightarrow {}^3H_5$, (c) $^3H_6 \rightarrow {}^3H_4$ and (d) $^3H_6 \rightarrow {}^3F_{2,3}$. O^{2-} mark peaks assigned to oxygen-assisted sites (after [54]), O_h – to cubic sites.

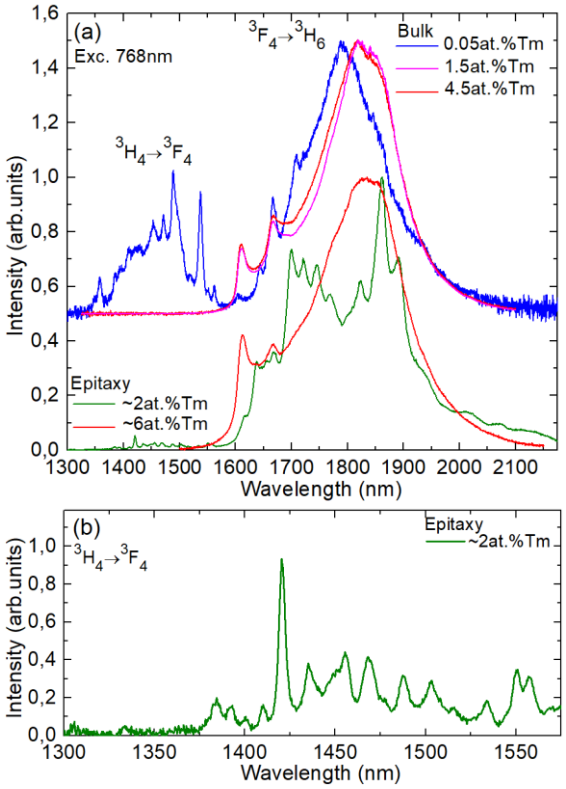

Figure 9. Near-IR RT luminescence of Tm^{3+} ions in LPE-grown Tm:CaF_2 thin-films: (a) overview spectra for the ~2 at.% and ~6 at.% Tm:CaF_2 layers, the spectra for bulk crystals are given for comparison; (b) a close look at the $^3H_4 \rightarrow {}^3F_4$ emission for the ~2 at.% Tm:CaF_2 layer. λ_{exc} = 768 nm.

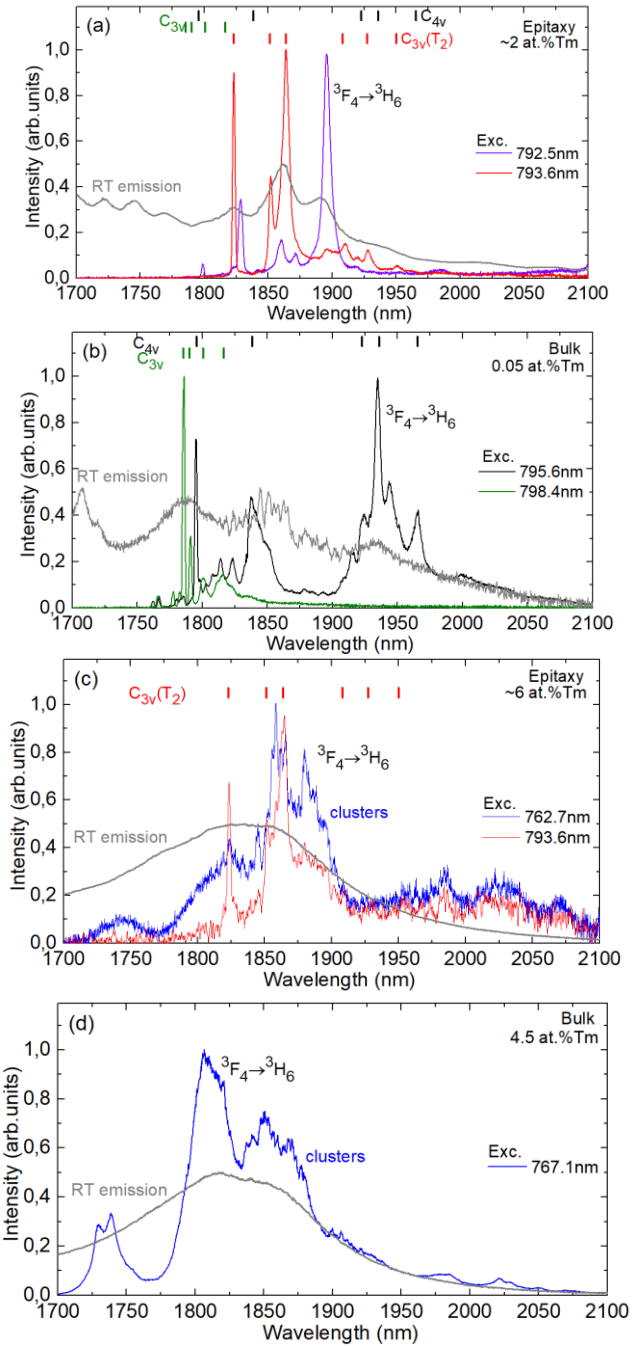

Figure 10. LT (12 K) luminescence spectra of Tm:CaF_2 epitaxial layers and bulk crystals corresponding to the $^3F_4 \rightarrow {}^3H_6$ Tm^{3+} transition measured under spectrally-selective excitation: (a) epitaxy, ~2 at.% Tm, (b) bulk crystal, 0.05 at.% Tm, (c) epitaxy, ~6 at% Tm and (d) bulk crystal, 4.5 at.% Tm. *Grey curves* – RT emission spectra (measured under non-selective excitation), *vertical dashes* – theoretical positions of electronic transitions for Tm^{3+} ions in C_{3v}, C_{4v} and $C_{3v}(T_2)$ sites in CaF_2.

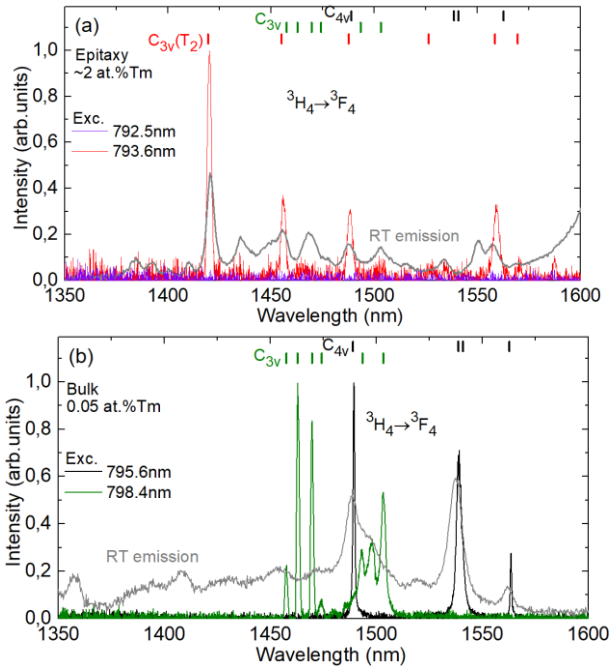

Figure 11. LT (12 K) luminescence spectra of (a) ~2 at.% Tm:CaF_2 epitaxial layer and (b) 0.05 at.% Tm:CaF_2 bulk crystal corresponding to the $^3H_4 \rightarrow {}^3F_4$ Tm^{3+} transition measured under spectrally-selective excitation. *Grey curves* – RT emission spectra (measured under non-selective excitation), *vertical dashes* – theoretical positions of electronic transitions for Tm^{3+} ions in C_{3v}, C_{4v} and $C_{3v}(T_2)$ sites in CaF_2.

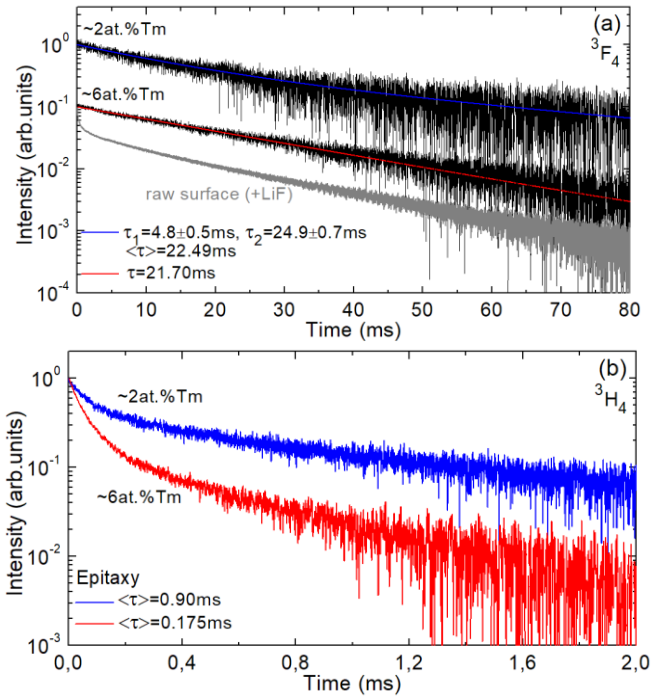

Figure 12. RT luminescence decay curves for LPE-grown polished Tm:CaF_2 thin-films: (a) emission from the $^3F_4$ state, λ_{lum} = 1830 nm; (c,d) emission from the $^3H_4$ state, λ_{lum} = 809 nm. λ_{exc} = 765 nm. In (a), the decay curve measured from the raw (as-grown) surface of the epitaxy is shown for comparison.

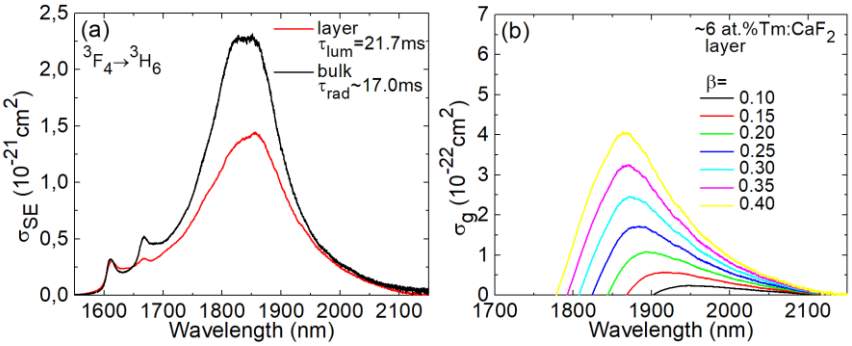

Figure 13. RT emission properties of Tm^{3+} ions in LPE-grown ~6 at.% Tm:CaF_2 thin-films: (a) stimulated-emission cross-sections, σ_{SE}, for the $^3F_4 \rightarrow {}^3H_6$ transition; the spectrum for bulk crystal is given for comparison; (b) gain cross-section, $\sigma_g = \beta\sigma_{SE} - (1-\beta)\sigma_{abs}$, spectra for various inversion ratios $\beta = N_2(^3F_4)/N_{Tm}$.

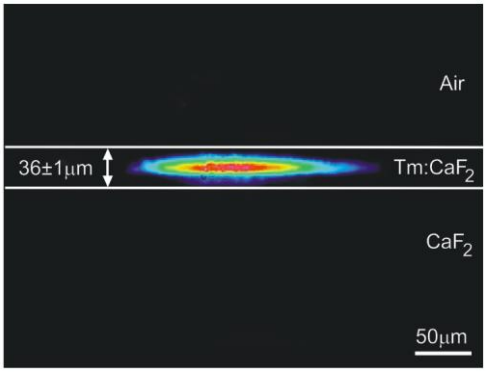

Figure 14. Near-field profile of the guided pump mode at 770 nm for the Tm:CaF_2 / CaF_2 epitaxy, *white lines* mark layer / substrate and layer / air interfaces.

Table 1. Absorption oscillator strengths* for Tm^{3+} ions in the ~6 at.% Tm:CaF_2 epitaxial thin-film.

$^3H_6 \rightarrow {}^{2S+1}L_J$	Γ, $cm^{-1}\times nm$	E_J, cm^{-1}	f_{exp} $\times 10^6$	$f^2_{calc}\times 10^6$	
				J-O	mJ-O
$^3F_4$	243.92	6096	*1.220***	0.800^{ED}	0.584^{ED}
$^3H_5$	129.95	8451	1.288	1.222^{ED}+ 0.423^{MD}	0.805^{ED}+ 0.423^{MD}
$^3H_4$	133.49	12832	2.974	1.564^{ED}	2.204^{ED}
$^3F_{2,3}$	89.48	14802	2.631	3.470^{ED}	3.642^{ED}
$^1G_4$	13.26	21602	0.844	0.245^{ED}	0.836^{ED}
$^1D_2$	28.68	28152	3.101	1.549^{ED}	3.098^{ED}
r.m.s. dev.				*0.880*	*0.369*

*Γ - integrated absorption coefficient, E_J – barycenter energy of absorption band, f_{exp} and f^2_{calc} - experimental and calculated absorption oscillator strengths, respectively (ED + MD). ED and MD stand for electric-dipole and magnetic-dipole contributions, respectively.

**The transition to the $^3F_4$ state was not considered.

Table 2. Intensity parameters for Tm^{3+} ions in the ~6 at.% Tm:CaF_2 epitaxial thin-film.

Model	$\Omega_k\times 10^{20}$, cm^2			$\alpha\times 10^4$, cm
	Ω_2	Ω_4	Ω_6	
J-O	0.003	1.080	1.637	–
mJ-O	3.833	1.449	2.569	0.269

Table 3. Probabilities of radiative spontaneous transitions* for Tm^{3+} ions in the ~6 at.% Tm:CaF_2 epitaxial thin-film (as calculated using the mJ-O theory).

Excited state	Terminal state	⟨λ⟩, nm	$A^{\Sigma}_{calc}(JJ')$, s^{-1}	$B(JJ')$, %	A_{tot}, s^{-1}	τ_{rad}, ms
$^3F_4$	$^3H_6$	1640	47.0^{ED}	100	47.0	21.30
$^3H_5$	$^3F_4$	4246	$5.17^{ED}+0.09^{MD}$	3.3	160.6	6.23
	$^3H_6$	1183	$101.8^{ED}+53.6^{MD}$	96.7		
$^3H_4$	$^3H_5$	2283	$16.3^{ED}+5.47^{MD}$	2.4	902.0	1.11
	$^3F_4$	1485	$82.5^{ED}+12.1^{MD}$	10.5		
	$^3H_6$	779.3	785.6^{ED}	87.1		
$^3F_3$	$^3H_4$	5447	2.18^{ED}	0.1	1924.9	0.52
	$^3H_5$	1608	206.2^{ED}	10.7		
	$^3F_4$	1166	$77.7^{ED}+30.6^{MD}$	5.6		
	$^3H_6$	681.7	1608.2^{ED}	83.5		
$^3F_2$	$^3F_3$	15106	$0.08^{ED}+0.10^{MD}$	<0.1	1580.0	0.63
	$^3H_4$	4002	15.3^{ED}	1.0		
	$^3H_5$	1454	323.5^{ED}	20.5		
	$^3F_4$	1083	485.4^{ED}	30.7		
	$^3H_6$	652.3	755.6^{ED}	47.8		
$^1G_4$	$^3F_2$	1595	26.3^{ED}	0.8	3255.3	0.31
	$^3F_3$	1442	$156.3^{ED}+2.62^{MD}$	4.9		
	$^3H_4$	1140	$444.7^{ED}+20.4^{MD}$	14.3		
	$^3H_5$	760.4	$1388.6^{ED}+80.2^{MD}$	45.1		
	$^3F_4$	644.9	$285.5^{ED}+6.19^{MD}$	9.0		
	$^3H_6$	462.9	844.4^{ED}	25.9		

*⟨λ⟩ - calculated mean emission wavelength, A^{Σ}_{calc} – probability of radiative spontaneous transitions (ED + MD), B(JJ') – luminescence branching ratio, A_{tot} and τ_{rad} – total probability of radiative spontaneous transitions (ED+MD) and radiative lifetime of the excited state, respectively. ED and MD stand for electric-dipole and magnetic-dipole transitions, respectively.